Coastal Engineering 211 (2026) 105087

Contents lists available at ScienceDirect

Coastal Engineering

journal homepage: www.elsevier.com/locate/coastaleng

Hydrodynamics of dam-break waves on grass slopes: Experiments and comparison with overtopping flows

Davide Wüthrich [a,*], Anne Mozer [b], Holger Schüttrumpf [b]

[a] Department of Hydraulic Engineering, Delft University of Technology, the Netherlands
[b] Institute of Hydraulic Engineering and Water Resources Management, RWTH Aachen University, Aachen, Germany

ARTICLE INFO

Keywords:
Dam-break waves
Wave overtopping
Hydrodynamics
Vegetation roughness
Experimental hydraulics

ABSTRACT

Highly unsteady air-water flows are common in coastal and hydraulic engineering, particularly during dike breaches and wave overtopping events, where sudden releases of water propagate down on slopes. Despite their relevance in erosion processes, structural stability and human safety, the hydrodynamic behaviour and multiphase characteristics of these unsteady flows remain poorly understood. This study presents new experiments on dam-break waves propagating over smooth and grass-covered slopes with a 1:3 inclination, representative of typical dikes in north-western Europe. The experiments were conducted using a dam-break facility equipped with ultrasonic distance sensors and high-speed imaging to capture wave-front celerities and flow depths. Results show that surface roughness substantially influences wave propagation, leading to reduced celerities and enhanced air entrainment. On vegetated slopes, a highly aerated "*white-water*" front developed, extending over a distance equal to 5 times the dam's impoundment depth, followed by a gradual decay of aeration. The measured wave front celerities agreed well with previous analytical solution for dam-break flows on slopes using friction factors consistent with steady flows on artificial grass. Ensemble-averaged flow depth data from up to 320 repetitions revealed statistically robust patterns of free-surface fluctuations. Results also provided a comparison between dam-break waves and unsteady flows generated with the Wave Overtopping Simulator (WOS), showing similarities and highlighting differences. Overall, these findings improve our understanding of multiphase unsteady flows on vegetated slopes and provide valuable data for developing more accurate predictive models for flood impacts and coastal structure design.

1. Introduction

Highly unsteady flows are common in coastal and hydraulic engineering, particularly in situations involving sudden releases of water. These events may occur in a wide range of contexts, including the failure of natural or man-made dams and dike breaches (Ritter, 1892; Froehlich, 2016). Surging waters can also be the result of faulty or uncontrolled operations of hydraulic infrastructure which may result in the overtopping of rivers, waterways and lakes. Unsteady flows also follow extreme water events, including (flash)floods, storm surges, tsunamis or Glacier Lake Outburst Floods (GLOF), with evidence showing that such flows have historically led to severe damage and significant loss of life (Hamlet and Lettenmaier, 2007). In coastal engineering unsteady flows on dikes occur after wave overtopping and overflow, when water levels exceed the crest of a structure. Despite their different origins, these flows share a common feature: a rapid release of water that propagates along a crest or down a slope, generating strongly unsteady flow conditions, including a sudden discontinuity and extremely rapid variations of flow depth and velocity (Chanson, 2005).

Once initiated, these flows evolve along the (grass) slope in ways that remain poorly understood. Because of roughness and high flow resistance, these unsteady flows often generate a broken wave front that becomes highly turbulent and consists of a mixture of air, water and sometimes sediments (Fig. 1). In coastal engineering this turbulent mixture is commonly referred to as "*white water overtopping*" due to its appearance, showing fascinating interactions of air and water, that alter fluid properties and momentum exchange within the flow (Schüttrumpf and Oumeraci, 2005; Chanson, 2005; Wüthrich et al., 2021). These multiphase, turbulent flows can have significant consequences, as they are possibly responsible for dike erosion, generate additional or modified loads on infrastructure and induce scour around structures (EurOtop, 2018). Furthermore, they can lead to downstream flooding

* Corresponding author.
E-mail address: d.wuthrich@tudelft.nl (D. Wüthrich).

https://doi.org/10.1016/j.coastaleng.2026.105087
Received 4 February 2026; Received in revised form 4 June 2026; Accepted 6 June 2026
Available online 7 June 2026
0378-3839/© 2026 The Authors. Published by Elsevier B.V. This is an open access article under the CC BY license (http://creativecommons.org/licenses/by/4.0/).

and pose serious safety risks to people, endangering their stability and preventing evacuation (van der Meer et al., 2022;Wüthrich et al., 2022), as shown in Fig. 1c.

While coastal design practices account for overtopping volumes (e.g. Goda, 2000), these unsteady flows on slopes have not been thoroughly explored and their hydrodynamic behaviour remains poorly understood, particularly their multiphase (air-water) nature, which may result in air-induced drag-reduction (Chanson, 1994) and affect hydrodynamic processes such as wave propagation, erosion, scour and impact loads on infrastructure. To fill this gap, this study provides new detailed experimental observations on the hydrodynamic behaviour of dam-break waves on grass slopes, offering new insights into their underlying physical processes, and enabling a comparison with non-impulsive wave overtopping, more widely studied in coastal engineering. This is expected to lead to a more unified understanding of highly unsteady, air-water flows on grass-covered slopes.

2. Literature review

Dam-break waves are generated by the sudden release of a water volume, propagating downstream in an uncontrolled manner. These highly unsteady and potentially dangerous flows share fundamental characteristics with tsunamis and storm surges (Chanson, 2006; Xu et al., 2023), as well as overtopping waves on inclined dikes (Bagg et al., 2025). Such similarities include unsteady propagation and a free-surface singularity at the front, leading to self-aeration and air entrainment.

2.1. Dam-break waves

Dam-break waves have been studied in the past, with most research focusing on their propagation over horizontal beds. The first analytical solution was developed by Ritter (1892), who employed the method of characteristics to derive a closed-form 1D solution of the Navier-Stokes equations for a semi-infinite reservoir of heigh d_0, filled with an ideal fluid, whose failure generates a dam-break wave on a horizontal and frictionless bed. With this model, dam-break waves can be described by flow depth h (x,t) and velocity v (x,t), both varying with space x and time t (Lauber and Hager, 1998; Chanson, 2009):

$$h = \frac{1}{9g}\left[2\sqrt{gd_0} - \frac{x}{t}\right]^2 \quad [1a]$$

$$v = \frac{2}{3}\left[\sqrt{gd_0} + \frac{x}{t}\right] \quad [1b]$$

Together, these parameters allow to calculate the discharge flowing out from the reservoir, given by $Q = hvB$, where B is the channel width. Ritter's theory allows to determine the flow depth and discharge at the gate location ($x = 0$), resulting in equations that depend only on dam height (or impoundment depth) d_0, channel width B and gravitational constant g (here $g = 9.81$ m/s^2):

$$h_0(x=0) = \frac{4}{9}d_0 \quad [2]$$

$$Q_0(x=0) = q_0 B = h_0 v_0 B = \frac{8}{27}Bd_0\sqrt{gd_0} \quad [3]$$

According to (Ritter, 1892) the wave front propagates with a celerity U

$$U = 2\sqrt{gd_0} \quad [4]$$

Eq. [4] applies to ideal fluids propagating on smooth horizontal beds, representing an idealized (upper-bound) scenario. The effects of bed



Fig. 1. Overtopping waves in prototype and large-size facilities: (a) Wave Overtopping Simulator WOS in the Hedwige-Prosperpolder (image by D.Wüthrich); (b) overtopping events during a flood in 1936 (image by F.Zitscher) and (c)People stability under overtopping waves during the study by (Wüthrich et al., 2022).

roughness have been investigated by several researchers, including Dressler (1952) and Whitham (1955). However, these theories become less accurate for larger time scales and do not apply to macro-roughness. Escande et al. (1961) specifically studied the influence of bed roughness on dam-break waves in natural valleys, while Chanson (2006) showed that dam-break waves can be used to simulate tsunamis propagating inland. Additional studies provided experimental evidence that the wavefront assumes a rounded shape (Whitham, 1955; Chanson, 2009) and that its celerity coefficient $U/(gd_0)^{0.5}$ is less than 2 for rough beds (e.g. Wüthrich et al., 2018). To compute these wave front celerities, Nielsen et al. (2022) demonstrated that dam-break waves over rough beds exhibit characteristics similar to breaking bores, allowing an intriguing comparison with Stoker's (1957) shock theory. This allows to estimate the celerity as a function of bed roughness using a Taylor expansion, yielding excellent alignment with experimental data. Xu et al. (2023) showed that dam-break waves over a horizontal grass bed exhibit complex dynamics and significant air entrainment. More specifically, their experimental study investigated the boundary layer near the dam-break wave tip on a dry, rough, horizontal bed, providing detailed measurements of horizontal velocities and bed shear stresses. Results revealed approximately uniform velocity profiles at the wave tip (in line with Wüthrich et al., 2018), accompanied by an initial peak in bed shear stress, followed by a rapid decline further downstream, where velocity profiles became depth-dependent (Xu et al., 2023). Despite these advances, the knowledge on the boundary layer development in dam-break waves remains poorly understood and further studies are needed.

Dam-break waves on **sloping beds** have been investigated by various researchers. Among them, Dressler (1952, 1958), Sakkas and Strelkoff (1973,1976) and Chen and Armbruster (1980) applied the method of characteristics to derive numerical solutions for dam-break problems on inclined beds, though they all encountered challenges at the leading edge. Hunt (1982, 1984) examined dam-break waves down a sloping channel and introduced an analytical solution of the kinematic wave equation, which becomes valid once the wave has propagated approximately four reservoir lengths (defined by Hunt, 1982 as $L = d_0/S_0$) downstream of the dam location. Hunt's (1982) solution presents equations to predict the wave front celerity U as a function of the Darcy friction factor f, incorporating factors such as the uniform equilibrium flow velocity V_H (corresponding to a water depth equal to the impoundment depth d_0), bed slope S_0, position of the front x_s (measured from the dam site), and time t

$$V_H = \sqrt{\frac{8g}{f} d_0 S_0} \quad [5a]$$

$$\frac{U}{V_H} = -\frac{3}{4}\frac{V_H t}{L} + \sqrt{\frac{x_s + L}{L} + \left(\frac{3}{4}\frac{V_H t}{L}\right)^2} \quad [5b]$$

The developments of Hunt (1982, 1984) were validated by many experimental studies, including those by Nsom et al. (2000) and Chanson (2004a,b). A summary of previous experimental studies on dam-break waves on a slope is presented in Table 1. More specifically, Nsom et al. (2000) investigated dam-break waves downstream of a finite reservoir in horizontal and sloping channels with very viscous fluids, revealing an initial phase dominated by inertial forces, followed by a shift to viscous effects. Mungkasi and Roberts (2011) analytically solved dam-break wave propagation on dry sloped beds using the method of characteristics, while Liu et al. (2020) examined dam-break waves across various slopes and downstream water levels. Melis et al. (2019) studied dam-break waves on slopes covered in dense vegetation. Numerous numerical studies, such as Wang and Pan (2015), have also addressed the dam-break problem, with Ancey et al. (2008) providing an exact solution of ideal dam-break flows on steep-slope.

Table 1
Literature review of dam-break experiments (dry bed) on a slope and selected studies on the hydrodynamic behaviour of overtopping waves on grass slopes.

		d_0 [m]	Slope S_0 [-]	U [m/s]	Friction	Note
Dam-break waves	Hunt (1982)	0.40	1:23.3 (2.5°)	0.79	$f = 0.09$ (concrete)	Theoretical development and comparison with experiments
	Nsom et al. (2000)	0.055	<12°	-	-	Very-viscous fluids (glucose syrup-water solutions)
	Chanson (2004a,b)	0.195-0.297	3.4 – 4°	1.97 - 2.43	$f = 0.05$ (stepped chute)	Air-water measurements and comparison with theory
	Melis et al. (2019)	0.15-0.30	0- 3%	-	$n = 0.05$ (Manning)	Rigid Stagged Vegetation (RSV)
	Liu et al. (2020)	0.20-0.40	0 – 2%	1.7 - 2.8	-	Dry bed data ($\alpha = 0$)
	Present study	0.20-0.40	1:3 (18°)	2.2 - 4.5	$f = 0.02$-0.2 (artificial grass)	
Overtopping waves	Van der Meer et al. (2010)	Overtopping Simulator	1:3.7 then 1:5.2	1 - 8	Grass	$h_{max} = 0.133 \cdot V^{0.50}$ (at dike crest) $u_{max} = 5.000 \cdot V^{0.34}$
	Bakker et al. (2011)	Overtopping Simulator	1:4 (top), 1:3 (middle), 1:2.5 (bottom)	3 - 10	Grass	Experiments in Tholen (the Netherlands)
	Bakker et al. (2013)	Overtopping Simulator	1:3	3.8 - 9.5	Grass	Experiments in Millingen a/d Rijn (the Netherlands)
	Van der Meer et al. (2022)	Overtopping Simulator	1:3	2 - 8	Grass	Tests focused on people stability
	Hughes (2015) Hughes and Thornton (2016)	Overtopping Simulator	1:3 or 1:6	-	Grass	*FlowDike* experiments (5 799 tests): $h_{max} = 0.324 \cdot V^{0.50}$ $u_{max} = 27.67 \cdot (V \cdot \tan S_0)/T_{m-1,0}$ $q_{max} = 0.4858 \cdot V^{0.75} \cdot [g \tan S_0]^{0.5}$
	(Wüthrich et al., 2022)	Overtopping Simulator	1:3	3.1 - 7.7	Grass	*Polder 2C's* experiments at $x = 8$ m $h_{max} = 0.059 \cdot \ln(V)$ - 0.172 $U = 1.46 \cdot \ln(V)$-4.22
	Daamen et al. (2023)	Overtopping Simulator	1:2.9	2 - 9	Grass	*FutureDikes* experiments
	van der Vegt et al. (2024)	Overtopping Simulator	1:3, with intermediate horizontal part	4 - 9	Grass (asphalt in the horizontal part)	Experiments at *IJsselmeerdijk* (the Netherlands)

Note: Chanson (2004a,b) define d_0 as an equivalent dam-break impoundment depth, computed assuming Ritter solution at the inlet $d_0 = 9/4(Q^2/(gB^2))^{1/3}$ where Q is the discharge and B the channel width. For the Wave Overtopping Simulator V is the volume released per unit width [m^3/m]. Flow depth for (Wüthrich et al., 2022) is aerated.

2.2. Overtopping waves

Due to their relevance in multiple coastal processes, overtopping waves have been extensively studied across various scales, from small laboratory experiments to large prototype tests using the Wave Overtopping Simulator (Van der Meer, 2007) pictured in Fig. 1a. These Wave Overtopping Simulators (WOS) function on the principle that it is not essential to use real waves to replicate an overtopped bore. Instead, they can generate a controllable bore by directing water from a reservoir through a gate that is fully or partially raised (Van der Meer et al., 2007). Many empirical equations were introduced to characterise the hydrodynamic behaviour of these bores, linking maximum velocities u_{max} (or wave front celerity U) and flow depths h_{max} to the overtopped volume per unit length V in m^3/m (e.g. Van der Meer et al., 2010, 2022; Hughes, 2015, summarized in Table 1). Recently, Bagg et al. (2025) showed that (individual) overtopped bores generated by non-impulsive wave breaking can be replicated using dam-break waves. However, while the relationship between maximum flow depth and released volume is well captured, bore front celerities tend to be underestimated. Despite this, Bagg et al. (2025) highlighted that studies on the multiphase dynamics of unsteady flows on slopes are rare, and a quantitative measure of air content is lacking, limiting direct comparison between laboratory and prototype tests. This is confirmed by recent tests by van der Meer et al. (2022) and (Wüthrich et al., 2022) on pedestrian stability under overtopping waves, which emphasized the highly aerated and unsteady nature of these flows, reinforcing the need for further investigations into their (multi-phase) hydrodynamic characteristics.

3. Experimental set-up

All tests were conducted in a large size facility at the Institute of Hydraulic Engineering and Water Resources Management (IWW) of RWTH Aachen University (Germany). The dam-break gate was installed on top of an existing facility, previously used by Mozer and Harish (2024) and Mozer et al. (2025) for steady flow experiments. The flume had a width $B = 0.5$ m and the embankment had an angle of 18° (1:3 slope), which was based on common slopes for levees and dikes in the Netherlands and Germany [DIN 19712 (2013)]. The invert was covered with artificial grass with a stem height of 1.5 cm, and its roughness was estimated to vary between $f = 0.08$ and 0.3 according to Mozer and Harish (2024). The upstream reservoir was filled using the laboratory's pumping system, while water was evacuated from the downstream side of the ramp without interfering with the instrumentation.

3.1. Dam-break gate

Unsteady flows were generated using a dam-break facility with a lift gate to release the impounded volume. The gate was operated manually, but in all conditions it was opened quickly enough to meet the criteria set by Lauber and Hager (1998), ensuring that the wave propagation was unaffected by the gate's operation. The gate allowed for a maximum impoundment depth $d_0 = 0.4$ m, with a reservoir length of 2.9 m, resulting in a total stored volume of 0.58 m^3. The set-up and the main parameters are defined in Fig. 2.

3.2. Instrumentations

The dam-break waves propagating along the slope were investigated using three Ultrasonic distance Sensors (US) of type *Microsonic pico+35/I* with a measurement range of 70-600 mm, a resolution of 0.069-0.17 mm and a response time of 64ms. The sensors were installed in the flume centreline at three fixed positions $x = 2.2$ m, $x = 3.0$ m and $x = 3.8$ m, corresponding to $x/d_0 = 5.5$, 7.5 and 9.5 for the maximum impoundment depth $d_0 = 0.4$ m and sampled at 100 Hz. The US sensors were calibrated in situ and captured the wave's hydrodynamic behaviour, including flow depths h and wave front celerity, which was calculated based on the distance between consecutive US sensors and the travel time, $U_{US} = \Delta x/\Delta t$. Dam-break wave propagation was also recorded using high-speed videos (Kron Technologies Chronos 2.1 HD, 1,000fps), iPhone 13mini (240fps) and dSLR (Nikon D5500, f/2.8, 1/800s) cameras, used to document the air-water features in Section 4.

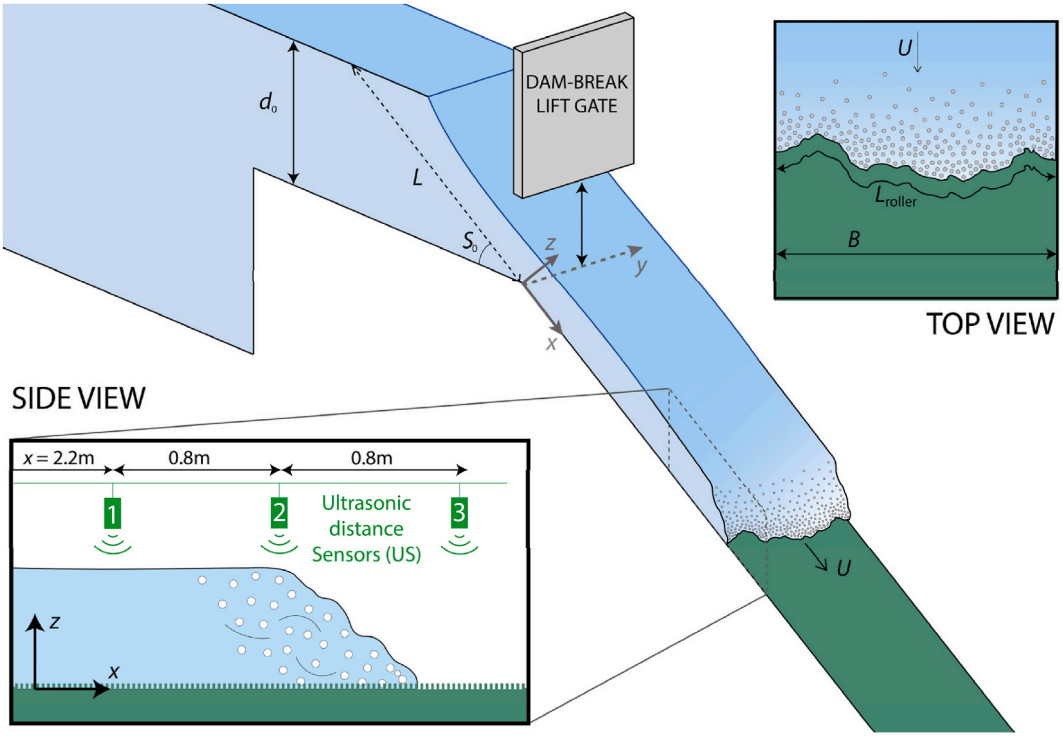


Fig. 2. Sketch of the experimental set-up, position of the instruments and definition of the main variables.

3.3. Methodology and test program

This study adopted a fully experimental approach, with the test program detailed in Table 2, including 3 flow conditions with impoundment depths d_0 in the range $0.2 < d_0 < 0.4$ m, all conducted on a '*dry*' bed, where '*dry*' refers to a grass surface that was slightly humid due to prior tests, but without any residual standing water. A minimum interval of 3 min was observed between repetitions, allowing all water to drain gravitationally down the slope. Analysis was conducted in two phases.

- **Phase 1** - Preliminary investigations were conducted using video analysis (240 fps) to characterise the main hydrodynamic features of the waves, including their celerity U along the chute from $x = 0$ to $x = 5$ m at 0.5 m intervals. Tests were performed for $d_0 = 0.2$, 0.3 and 0.4 m on both smooth and rough (grass) beds, with 4 to 7 repetitions for each flow condition (Table 2).
- **Phase 2** - A more detailed quantitative assessment of their hydrodynamic behaviour was performed for the rough (grass) bed for $d_0 = 0.2$, 0.3 and 0.4 m. This analysis included Ultrasonic distance Sensors (US) providing measurements of the wave front celerity U_{US} between US2 and US3, maximum depth h_{max} and time T_{max} at which it occurred. These tests were combined with air-water flow properties measurements, following the ensemble average methodology by Wüthrich et al. (2022a), which explains the large number of repetitions in Table 2. It is noted, however, that air-water flow measurements are not the objective of this study.

4. Visual observations

The sudden opening of the dam-break gate released water into the downstream flume, initiating a rapid flow over the slope. In the **smooth** bed configuration, the wave propagated with high celerities, reaching values up to 6 m/s. High-speed video footage revealed a very thin wave front with limited aeration, mainly due to minor surface irregularities at the invert (e.g. joints, tape). However, since such smooth surfaces are rare in real-world conditions, this configuration served as reference and only limited attention is given in the present study.

In contrast, dam-break waves propagating over a grass-covered slope exhibited a significantly different flow behaviour. As the waves skimmed over the grass, they entrained and entrapped air, generating a highly aerated flow. Aeration was particularly intense at the wave tip, where a mixture of air and water formed a visually prominent "*white water*" region, as illustrated in Fig. 3. Close-up views in Fig. 3a and b highlight a foamy mixture of air and water with heterogeneous bubbles moving along the grass surface, revealing complex air-water interactions in this zone. Fig. 3a and b reveal the presence of large bubbles interspersed with numerous smaller bubbles, suggesting vigorous turbulent mixing. High-speed video footage also captured dynamic patterns, including patches and "*scars*" on the free surface, indicative of strong free-surface turbulence, as previously noted by Brocchini and Peregrine (2001) and Wüthrich et al. (2021) in breaking bores, representing a comparable yet distinct type of unsteady flow.

The roller structure remained generally uniform behind the roller toe, but exhibited some irregularities in the transversal direction, resulting in an indented front profile (Fig. 3). The wave front tended to concentrate near the centreline, likely due to increased resistance along the sidewalls. A detailed quantification of the front profile during the early stages of the bore is provided in Section 5.3.

Aeration remained visually constant for a certain distance, then suddenly diminished, as indicated by a visible reduction in '*white water*'. This transition is clearly illustrated in Fig. 3c and d, where aeration progressively diminishes, and distinct air structures emerge from the bottom, similarly to the inception point of free-surface aeration in spillway flows (Chanson, 2024). The length of the fully aerated region L_{air} was estimated from top-view images (*e.g.* Fig. 3c and d) and it was observed to increase along the slope. For example, for a dam-break wave with an impoundment depth $d_0 = 0.3$ m, L_{air} was ~0.85 m at x ~2.2 m (US1), increased to ~1.2 m at $x = 3.8$ m (US3) and reached ~1.3 m at $x = 5.0$ m. Visual observations based on video recordings allowed to quantitatively reconstruct the development of the aerated region along the slope for three impoundment depths $0.2 < d_0 < 0.4$ m and data (averaged over all available videos) is presented in dimensionless form in Fig. 4, where one can see a clearly increasing behavior until a constant value $L_{air}/d_0 \sim 5$ is reached after $x/d_0 > 12$-15, which is consistent with celerity data in Section 5.1. All tested waves had a similar behavior, which was well represented by this expression, obtained as empirical best-fit:

$$\frac{L_{air}}{d_0} = 1.702 \ln \frac{x}{d_0} - 0.389 \qquad for \qquad 1.5 < \frac{x}{d_0} < 25 \qquad [6]$$

which gives an $R^2 = 0.98$ for all experimental data. For $x/d_0 < 1.5$ the wave was characterized by strong acceleration driven by the gate opening, without a clearly aerated front. It must be noted that these values are valid for grass slopes 1:3, since it is believed that both friction and slope will affect the air-water flow properties and therefore the characteristics of the bore front, hence resulting in modified coefficients in Eq. [6], for which additional tests on different surfaces and slopes are needed. Despite this, this trend suggests that the air-water interface plays a role in both the propagation of the bore, and the development of the boundary layer within the unsteady flow. Observations in the steady part of the flow revealed a lower level of aeration, aligning with previous observations on steady flows over similar surfaces (Mozer and Harish, 2024).

Table 2
Test program and flow conditions investigated in this study. Note that U_{US} was obtained using Ultrasonic distance Sensors (US), while U was calculated based on video analysis.

		d_0 [m]	Locations		U [m/s]	U_{US} [m/s]	T_{max} [s]	h_{max} [m]	Q_0/B [m^2/s]	Volume/m [m^3/m]	Reps.
Phase 1	**Smooth** (PVC)	0.2	0 to 5 m, $\Delta x = 0.5$ m	$0 < x/d_0 < 25$	4.28	-	-	-	0.083	0.58	4
		0.3	0 to 5 m, $\Delta x = 0.5$ m	$0 < x/d_0 < 16.7$	5.08	-	-	-	0.152	0.87	4
		0.4	0 to 5 m, $\Delta x = 0.5$ m	$0 < x/d_0 < 12.5$	5.27	-	-	-	0.234	1.16	5
	Rough (grass)	0.2	0 to 5 m, $\Delta x = 0.5$ m	$0 < x/d_0 < 25$	2.66	-			0.083	0.58	7
		0.3	0 to 5 m, $\Delta x = 0.5$ m	$0 < x/d_0 < 16.7$	3.46	-			0.152	0.87	6
		0.4	0 to 5 m, $\Delta x = 0.5$ m	$0 < x/d_0 < 12.5$	4.20	-			0.234	1.16	6
Phase 2	**Rough** (grass)	0.2	$x = 2.2$, 3.0, 3.8 m	$x/d_0 = 11$, 15, 19	-	2.35	1.55	0.048	0.083	0.58	160
		0.3	$x = 2.2$, 3.0, 3.8 m	$x/d_0 = 7.3$, 10, 12.7	-	3.81	1.65	0.062	0.152	0.87	320
		0.4	$x = 2.2$, 3.0, 3.8 m	$x/d_0 = 5.5$, 7.5, 9.5	-	4.44	1.55	0.075	0.234	1.16	320
										Tot	**828**

Note: for Phase 1 only video-based analysis was conducted, and no US data was recorded. U in Table 2 refers to video-based celerity at the most downstream measurement location $x = 5$ m; its evolution along the chute is shown in Fig. 5. In Phase 2, U_{US} is the celerity between US2 and US3.

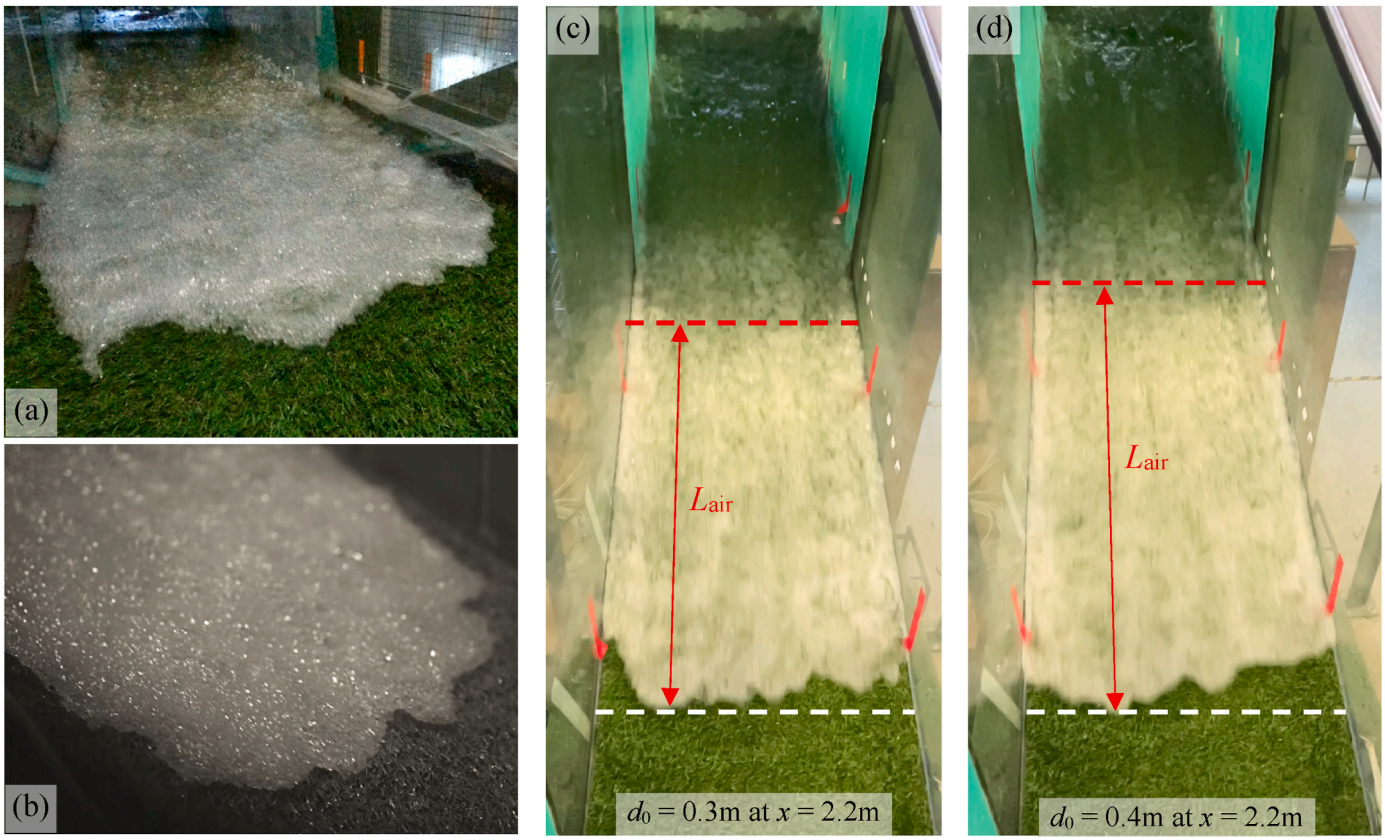


Fig. 3. Visual observations of the wave front for $d_0 = 0.40$m: (a) is a taken with a dSLR camera, while (b) was taken with a high-speed video-camera (1 000 fps, monochrome). (c),(d) top view images of the propagating waves, indicating the aerated flow region L_{air} at $x = 2.2$m for: (c) $d_0 = 0.3$m and (d) $d_0 = 0.4$m.

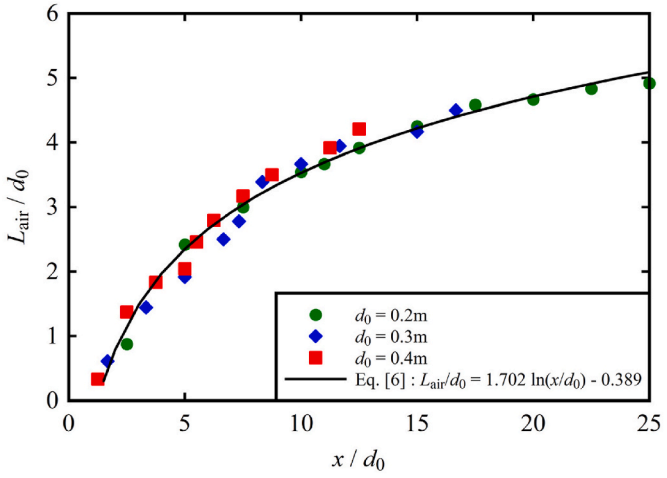


Fig. 4. Length of the aerated front L_{air} measured based on video observations for three flow conditions on grass-covered 1:3 slope. Experimental data show excellent agreement with the best-fit Eq. (6) ($R^2 = 0.98$).

5. Dam-break wave characteristics

This section discusses the main hydrodynamic properties of the dam-break waves on the sloping bed focusing on front celerity (Section 5.1), flow depths (Section 5.2) and wave's transversal profile (Section 5.3).

5.1. Wave front celerity

The dam-break waves were analysed for their celerity on both smooth (PVC) and grass-covered bottoms to enable comparison with literature. Wave front celerity U was extracted from 240fps video recordings, providing measurements at 0.5 m intervals along the chute. Videos were averaged on all available repetitions to enhance reliability of the results (Table 2). The findings were compared with data obtained from Ultrasonic distance Sensors positioned at $x = 2.2$, 3.0 and 3.8 m. The latter corresponded to $x/d_0 = 9.5$ for $d_0 = 0.4$ m, $x/d_0 = 12.7$ for $d_0 = 0.3$ m, and $x/d_0 = 19$ for $d_0 = 0.2$ m (Table 2). For grass-covered slopes, Fig. 5 shows an initial acceleration in the region $x/d_0 < 9$. The bore behaviour in the early stages is highly complex and not necessarily well described by hydrostatic models, as demonstrated by Stansby et al. (1998). Nevertheless, on grass slopes, the waves consistently accelerated until reaching a peak celerity, after which they decelerated toward a nearly constant value. This flattening part was only captured for $d_0 = 0.2$ m and 0.3 m, since for 0.4 m the flume was not sufficiently long. Such change in behaviour is believed to reflect a shift in dominant processes, with gravity controlling the initial phases, while friction increasingly governs the flow along the slope, where the flow tip becomes thinner and more aerated (see Section 5.2). In this second phase, excellent agreement is observed between experimental data for $d_0 = 0.3$ m and Hunt's (1982) theoretical solution in Eq. [5 b], which is not valid in the region $x/L < 4$ corresponding to $x/d_0 < \sim 12.7$, indicated in Fig. 5 by the grey-shaded area. A similar behaviour was observed by Chanson (2004b) for dam-break waves on stepped chutes, also reporting higher velocities in the initial steps, then decreasing toward a dimensionless wave front celerity at the end of the chute $U/(gd_0)^{0.5} \approx 1.5$, consistent with the present results. Chanson (2004b) further noted that this behaviour was more evident for larger discharges (i.e. higher impoundment depths), which aligns with trends in Fig. 5.

The wave front celerities at $x = 3.8$ m were compared in Fig. 6 with Eq. [5a] from Hunt (1982), showing good agreement with Darcy-Weisbach friction factors $0.02 < f < 0.2$ (red crosses). Although

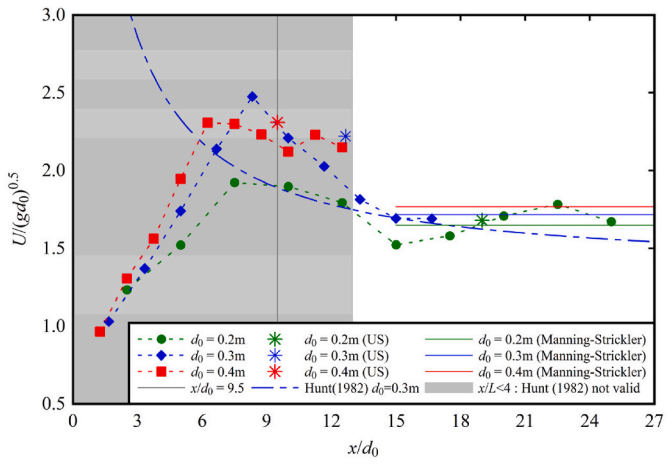


Fig. 5. Behaviour of the wave front celerity of dam-break waves along a 1:3 grass slope. Data for $d_0 = 0.3$m (blue symbols) are compared with the analytical solution by Hunt (1982) in Eq.[5*b*], which is valid *after*4 reservoir lengths downstream of the dam, here $x/d_0 > \sim 12.7$. Data is also compared to uniform flow calculations for $x/d_0 > 15$(continuous lines) with Manning-Strickler coefficient $n = 0.02\,s/m^{1/3}$. (For interpretation of the references to colour in this figure legend, the reader is referred to the Web version of this article.)

this range is relatively broad, it is consistent with values $0.08 < f < 0.3$ found by (Mozer and Harish, 2024) for steady supercritical flows on the same grass slope. In contrast, the EurOtop (2018) manual recommends a friction factor $f = 0.01$ for real grass-covered dikes on a 1:3 slope, which is lower than the values observed in the present study and possibly due to the differences in flow behaviour, including WOS's larger initial flow velocity in comparison to dam-break waves, further addressed in Section 6. For context, Chanson (2004a,b) found $f = 0.05$ for dam-break waves over a stepped chute, while Wüthrich et al. (2019) performed experiments on an artificial carpet (smoother than the present study) and found $f \approx 0.04$. For completeness, results are compared with the Altsul formula (Idelchik, 1969), that for the above flow conditions gives $0.039 < f < 0.044$. Although slightly less accurate, Altsul's formula offers an explicit expression that can be used to initiate calculations in the Colebrook-White formula (Chanson, 2009). It is also worth noting, as highlighted by Hunt (1982), that there is a '*tendency for f to increase under unsteady flow conditions*' due to steeper velocity gradients near the invert. While the present data show some consistency across all methods, they also highlight the need for more accurate theoretical models to estimate friction factors in unsteady flow conditions.

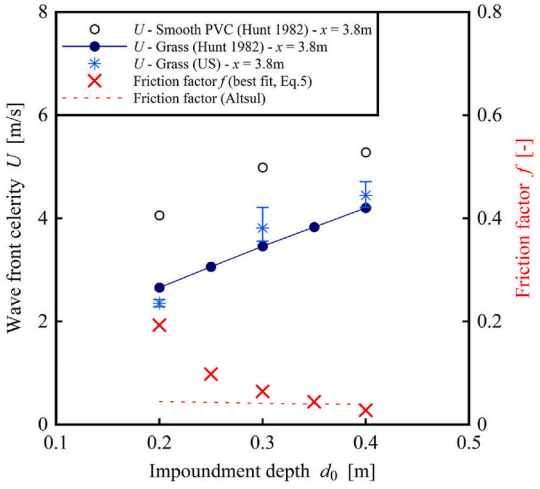


Fig. 6. Wave front celerity of dam-break waves at a fixed location $x = 3.8$ m on a 1:3 grass slope. Data is compared with the analytical solution by Hunt (1982) in Eq. [5b]. Friction factors are obtained as best fits with Eq. [5b].

Lastly, once the wave became fully developed (i.e. $x/d_0 > 15$) and gravitational and frictional forces balance each other, Fig. 5 shows good agreement with the uniform flow velocity $v = 1/n \cdot h^{2/3}\sqrt{S_0}$ solved for the flow depth, assuming a constant discharge Q_0 typical of dam-break waves (Eq. [3]) and a Manning-Strickler coefficient $n = 0.02\,s/m^{1/3}$, which is similar to $n = 0.0175\,s/m^{1/3}$ used by van Bergeijk et al. (2020) and van der Vegt et al. (2026). This shows that the bore front initially travelled faster than uniform flow, which might explain the deceleration later associated with the increase in flow depth, indicating that the initial stages of the wave propagation are controlled by gravity, in line with Hunt (1982). However, it must be noted that for the largest wave ($d_0 = 0.4$ m), the flume was not long enough to capture the wave's deceleration.

The celerity values in Fig. 6, obtained using Ultrasonic distance Sensors (US), include error bars derived from the 160 to 320 repetitions performed for the ensemble-averaged analysis of air-water flow properties. This large number of repetitions allowed for a statistical evaluation of the wave front celerity, presented in Fig. 7, where similar distributions across all configurations can be observed, along with a relatively narrow standard deviation, indicating good repeatability of the experiments.

5.2. Flow depths

Flow depths were measured at three locations along the chute using Ultrasonic distance Sensors (Table 2). The ensemble-averaged profiles at the most downstream location ($x = 3.8$ m) are presented in Figs. 8 and 9 for all tested flow conditions $d_0 = 0.20$, 0.30 and 0.40 m. A clear trend can be observed: the flow depth initially increases, reaches a maximum h_{max} at time $T = T_{max}$, with the values of T_{max} at $x = 3.8$ m listed in Table 2. The wave is then followed by a decrease at the end of the wave, which is consistent with previous studies.

Fig. 8 shows the evolution of the flow profiles along the chute, revealing that each location exhibits a slightly modified behaviour. First, the maximum depth h_{max} typically decreases between US1 and US2 and then increases at US3, except for $d_0 = 0.2$ m, where a monotonic increase is observed. These trends are consistent with the celerity data: the decrease between US1 and US2 reflects flow acceleration in the gravity-dominated region, while the subsequent increase between US2 and US3

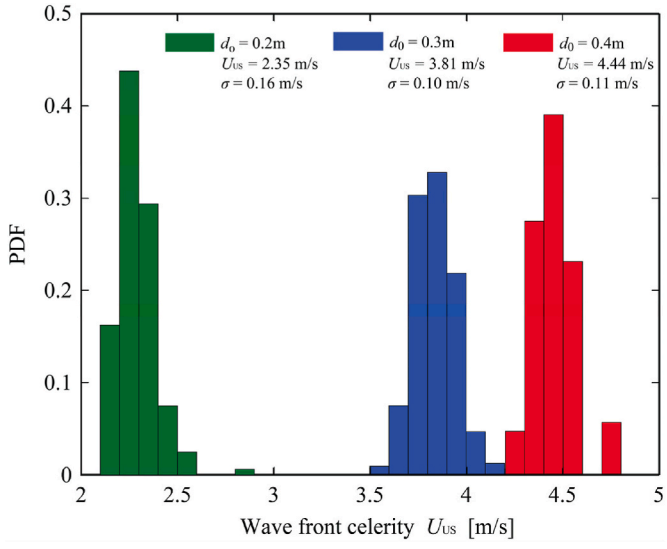


Fig. 7. Probability Distribution Functions (PDF) of the wave front celerities obtained from the Ultrasonic distance Sensors (US) at $x = 3.8$m, ensemble averaged over 320 repetitions for $d_0 = 0.3$ and 0.4m and 160 repetitions for $d_0 = 0.2$m. U_{US} is the mean values, while σ is the standard deviation.

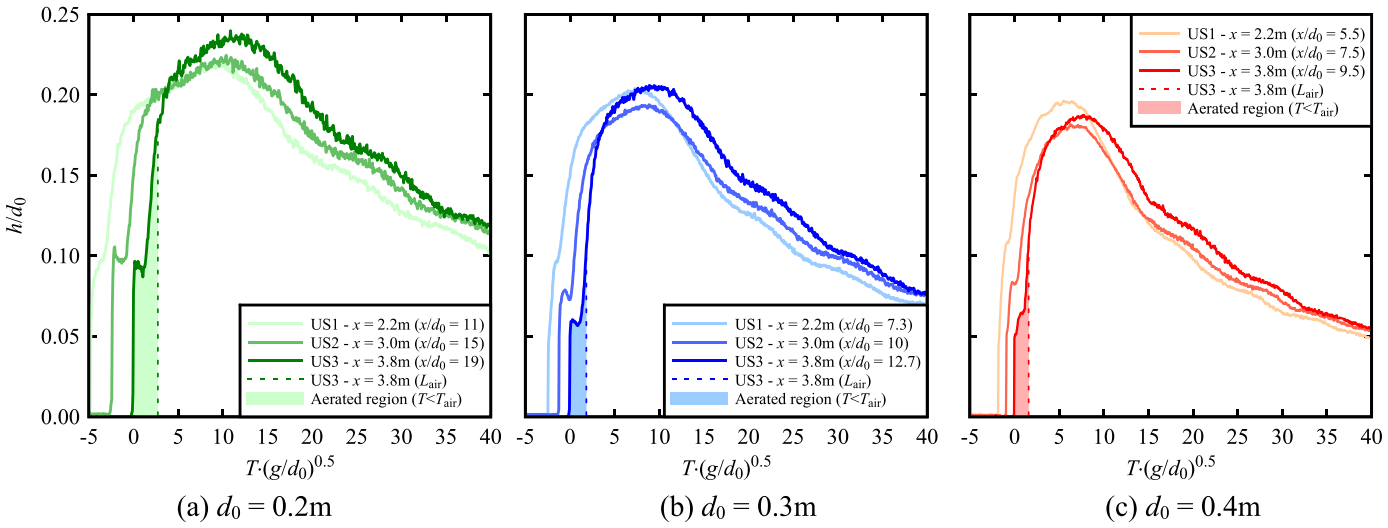


Fig. 8. Evolution of flow depths along the chute at the locations. Data is ensemble-averaged over 320 repetitions for $d_0 = 0.3$ m and 160 for $d_0 = 0.2$ m. The reference time $T = 0$s refers to the wave's arrival at US3 ($x = 3.8$ m).

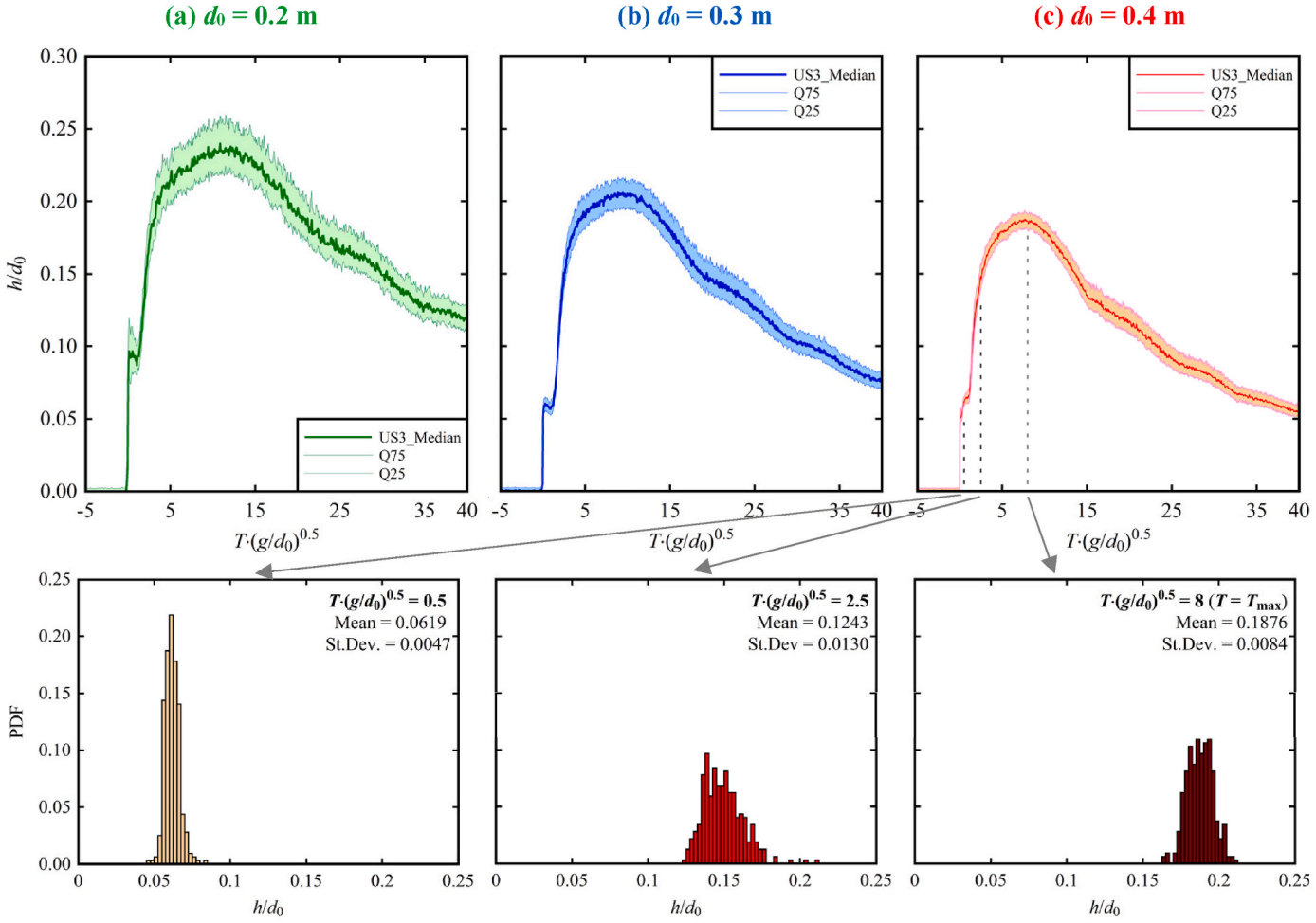


Fig. 9. Time histories of the flow depths obtained with Ultrasonic distance Sensors at $x = 3.8$ m, ensemble averaged over 320 repetitions for $d_0 = 0.3$ and 0.4 m and 160 repetitions for $d_0 = 0.2$ m. Coloured areas represent the difference between 25 and 75 quartiles. Lower graphs show the distribution of the fluctuations at 3 selected times for $d_0 = 0.4$ m.

corresponds to the friction-driven deceleration in Fig. 5. For $d_0 = 0.2$ m, the flow likely reaches a friction-dominated regime already at US1 ($x/d_0 = 11$), explaining the continuous increase in h_{max}. Second, in terms of temporal characteristics, the overall wave duration remains approximately constant along the chute, suggesting that diffusivity effects are limited within the investigated reach. Lastly, regarding the wave shape, the initial wave tip becomes more pronounced as the wave propagates along the chute, where the flow thins, likely due to gravity-

driven dynamics. Simultaneously the frictional effects locally intensify until an equilibrium is reached, after which the wave shape remains relatively unchanged, e.g. between US1 and US3 for $d_0 = 0.2$ mm which has reached fully developed conditions.

The results from the visual observations of the aerated region in Chapter 4 were compared with US data by obtaining an aerated time $T_{air} = L_{air}/U$ at $x = 3.8$ m, based on the experimental data in Fig. 4. This aerated region (or phase) is highlighted using shaded areas in Fig. 8. Data indicated that aeration extends beyond the tip region captured by the Ultrasonic distance Sensors, reaching into the rising part of the wave, more evidently for smaller waves with $d_0 = 0.2$ m. This shows that the appearance of white water is not necessarily confined to the wave tip identified by the Ultrasonic distance Sensors. However, this might be attributed to a combination of factors: (1) the conversion between spatial visual observations and temporal US measurements is obtained using the celerity U, which might not represent the local flow velocity at the inception point (which is lower), overestimating L_{air}; (2) visual observations are qualitative, limiting their accuracy; (3) visual observations of air-water flows are depth-averaged, which means that visible air could be located within the shear layer, with clear water above. This might suggest that surface aeration does not fully represent what happens within the bore and to solve this uncertainty intrusive measurements are required. Lastly, it remains unclear what US sensors actually measure in aerated flows: Wüthrich et al. (2021) and (Regout et al., 2026) reported that US surface data in breaking bores corresponded to void fractions of ~70% (*i.e.* 70% air, 30% water), but such data need to be combined with detailed (intrusive) air-water flow measurements. Altogether, clarifying these processes is important to understand multi-phase flow dynamics at the interface between waves and the bottom slope (e.g. grass or soil), fundamental for dike erosion and stability.

Many repetitions were performed (160 for $d_0 = 0.2$ m and 320 for $d_0 = 0.3$ and 0.4 m). This extensive dataset allowed to characterise the statistical behaviour of the free-surface fluctuations, with the upper (Q75) and lower (Q25) quartiles shown as shaded regions in the top row of Fig. 9. Overall, the fluctuations remained relatively constant throughout the wave, with the narrowest distributions observed near the leading edge and the widest occurring during the rising limb near the maximum depth. This trend is illustrated in the bottom row of Fig. 9, which shows the pdf distributions of fluctuations at three selected time instants for $d_0 = 0.4$ m.

5.3. Wave transversal profile

Dam-break waves are commonly simplified as 1D processes, assuming uniform flow in the transversal direction. In reality, this is not the case (e.g. Fig. 1), and deviations can be quantified using the indentation coefficient I_c, defined as the ratio between the roller perimeter (L_{roller}, sketched in Fig. 2) and the channel width, here $B = 0.5$ m. This parameter I_c provides a quantifier for the 2D behaviour of the flow and associated fluctuations in the transversal y direction. Therefore, $I_c = 1$ represents an idealized straight line perpendicular to the channel axis (Wüthrich et al., 2020). Following this approach, the wave transversal profiles were extracted from video recordings and I_c was computed as the measured length of the front profile L_{roller}, divided by $B = 0.5$ m. All datapoints are averaged over 3 videos to ensure maximum reliability and minimize local effects. Results are presented as a function of the longitudinal distance x from the gate location, normalised by the dam's impoundment depth d_0. Data for the **smooth** configuration in Fig. 10a showed initial values I_c ~1.1, which increased along the chute with some oscillations. All tests revealed a local minimum for $x/d_0 \sim 8$, after which I_c stabilized around a mean value of 1.3-1.4 for all configurations.

The **rough** (grass) configuration displayed slightly different behaviour compared to the smooth case, revealing a slightly higher initial value of $I_c \sim 1.3$ immediately downstream of the gate. A minimum I_c of 1.1-1.2 was reached for $x/d_0 = 5$ to 8 which coincides with the deceleration in Fig. 5 and the transition from gravity to friction dominated process. This is followed by a steady increase to ~1.8 for all tested configurations, possibly attributed to: (1) the presence of aeration at the front (Fig. 3) and (2) an elongation of the profiles in the centre, occasionally accompanied by non-symmetrical behaviour due to the presence of roughness on the slope. Importantly, these values approach those observed in prototype experiments such as the Wave Overtopping Simulator ((Wüthrich et al., 2022); Daamen et al., 2023; van der Vegt et al., 2024), further discussed in Chapter 6.

6. Discussion: comparison with overtopping waves

This study investigated dam-break waves propagating over a grass-covered slope, resulting in highly unsteady and turbulent flows that share both similarities and differences with individual (non-impulsive) overtopping waves. These phenomena are of great relevance in coastal

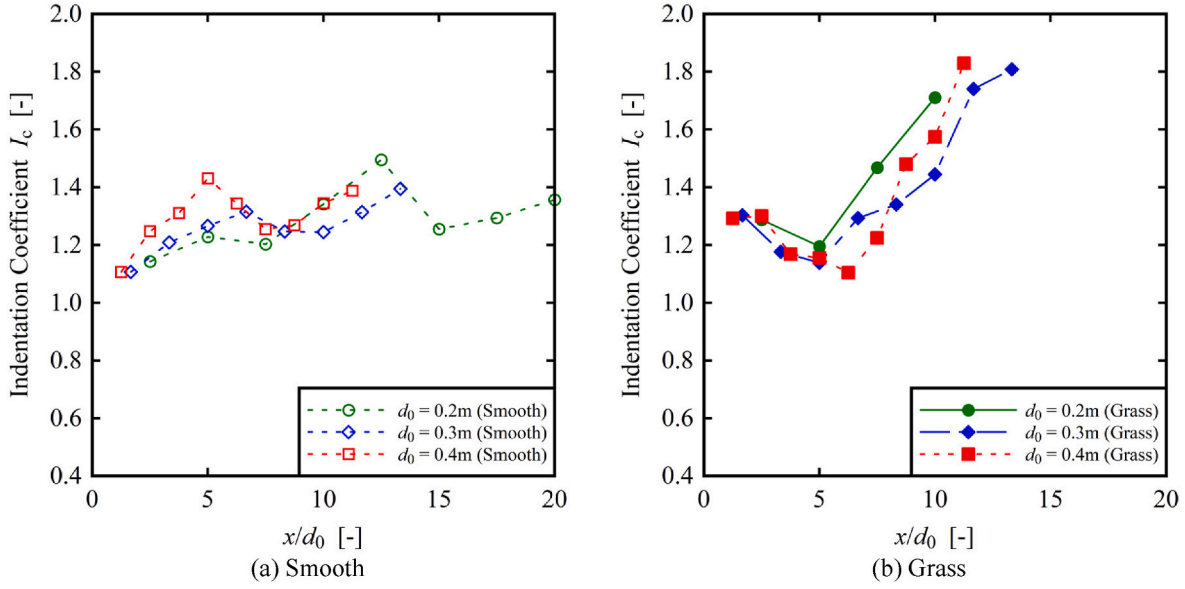


Fig. 10. Evolution of the indentation coefficient I_c as function of the longitudinal channel distance for (a) smooth; and (b) grass slope. I_c is defined as the ratio between the roller length L_{roller} and channel width B, i.e. $I_c = L_{roller}/B$.

engineering and have been extensively studied in the past (Section 2.1). Overtopping waves are often reproduced using Wave Overtopping Simulators (EurOtop, 2018; van der Meer et al., 2007, 2010, 2022), as shown in Fig. 1a, where the simulator replicates the time-varying flow depth and velocity at the dike crest for a given overtopping volume (van der Meer et al., 2007). A connection between individual WOS-generated waves and dam-break waves was recently made by Bagg et al. (2025) for laboratory-generated bores on a horizontal flume, pointing out interesting similarities and differences between these two release mechanisms. This comparison is further explored herein for dam-break waves on an inclined 1:3 grass slope. Establishing this analogy requires linking the impoundment depth d_0 to the released volume per unit width [m^3/m], here calculated as $0.58 m^3/0.5 m = 1.16 m^3/m$ for $d_0 = 0.4$ m (Table 2). Using this approach, dam-break wave data (specifically, maximum water depths h_{max} and wave front celerities U) can be compared to empirical equations derived from the *FlowDike* experiment (Hughes, 2015), the Wave Overtopping Simulator by Van der Meer et al. (2010, 2022), *Polder2Cs* experiments ((Wüthrich et al., 2022)), *FutureDike* experiments (Daamen et al., 2023), experiments at Tholen and Millingen a/d Rijn (Bakker et al., 2011, 2013), as well as flume experiments by Bagg et al. (2025) for non-impulsive wave overtopping.

In terms of **maximum water depths** h_{max}, the present dam-break results are generally lower than most previous studies (Fig. 11a), but they align well with tests by Van der Meer et al. (2010), particularly during the initial bore propagation phase (i.e. 2 to 4 m downstream of the slope), despite the latter being conducted on a milder 1:3.7 slope. A closer analysis also reveals a difference in shape: WOS-generated waves are typically characterised by a rapid increase in flow depth, with the maximum occurring near the wave tip, often resulting in a triangular profile (e.g. van der Vegt et al., 2026), whereas dam-break waves show a more gradual and smoother increase in flow depth (e.g. Figs. 8 and 9). The present dam-break **wave front celerities** ranged between 2 and 4 m/s, in good agreement with laboratory experiments of Bagg et al. (2025) and can be well described by their empirical formulation $U = 3.673 \cdot V^{0.278}$. However, these values are lower than WOS data, where celerities typically range between 4 and 6 m/s for volumes comparable to the dam-break laboratory conditions (Fig. 11b). This difference can be attributed to the non-zero initial velocities at the crest for WOS waves, whereas dam-break waves originate from an impounded volume initially at rest (Ritter, 1892). For completeness, the maximum bore **flow rate** q_{max} for dam-break waves (computed using Ritter, 1892, Eq. [3]) was compared with WOS (computed following Hughes and Thornton, 2016, Table 1). The latter gives significantly higher values, consistent with previous findings by Bagg et al. (2025).

The wave propagation along the slope also showed interesting features, worth comparing. The present study identified two distinct zones: an initial gravity-dominated region, followed by a zone where friction becomes dominant (Section 5.2). A similar behaviour was reported by van der Vegt et al. (2026) for WOS wave, where an initial acceleration due to gravity leads to a reduction in flow depth, also observed in dam-break waves (Fig. 8). Subsequently, both flows revealed increasing friction effects, until they become comparable to gravitational forces and can be reasonably described using classical Manning-Strickler formulations. However, this transition from the gravity-dominated to the friction-dominated regime may occur at different longitudinal distances due to different initial velocities and flow conditions. Despite these similarities, friction coefficients differed, with WOS waves exhibiting lower values, justifying the lower EurOtop recommendations. This is also aligned with Fig. 6, where friction decreases with increasing wave front celerity and flow depth, likely linked to the higher velocities and depths in WOS waves, as well as their non-zero initial velocities at the crest.

The indentation coefficient $I_c = L_{roller}/B$ is a parameter that indicates how much the wave-front deviates from an idealized straight front. It was presented and discussed in Section 5.3 for dam-break waves (Fig. 10), but here compared with those extracted from prototype overtopping waves generated with WOS with volumes up to 2 m^3/m. This comparison is based on the data from (Wüthrich et al., 2022), *FutureDikes* experiments (Daamen et al., 2023) and tests at Ijsselmeerdijk (van der Vegt et al., 2024). For these large-scale overtopping cases, the aerated wave front was highly fragmented and dominated by irregular air-water protrusions, preventing accurate contour detection. Therefore, the perimeter was determined from the envelope of the aerated region (e.g. Fig. 12a and b) and the evolution of the indentation coefficient I_c along the flume is shown in Fig. 12d. At the beginning ($x = 2$ m) the data exhibited relatively scattered values, likely associated with the release mechanism and/or the change in slope. At $x = 4$ m, similar values I_c ~1.35-1.45 were observed for all released volumes, after which I_c constantly increased along the chute, reaching values of I_c ~1.8-2.0. This trend closely resembles that observed for dam-break waves in Fig. 10b, where I_c decreased to 1.2 before increasing again to 1.8. For the *Polder2C*'s data ((Wüthrich et al., 2022)), measured at

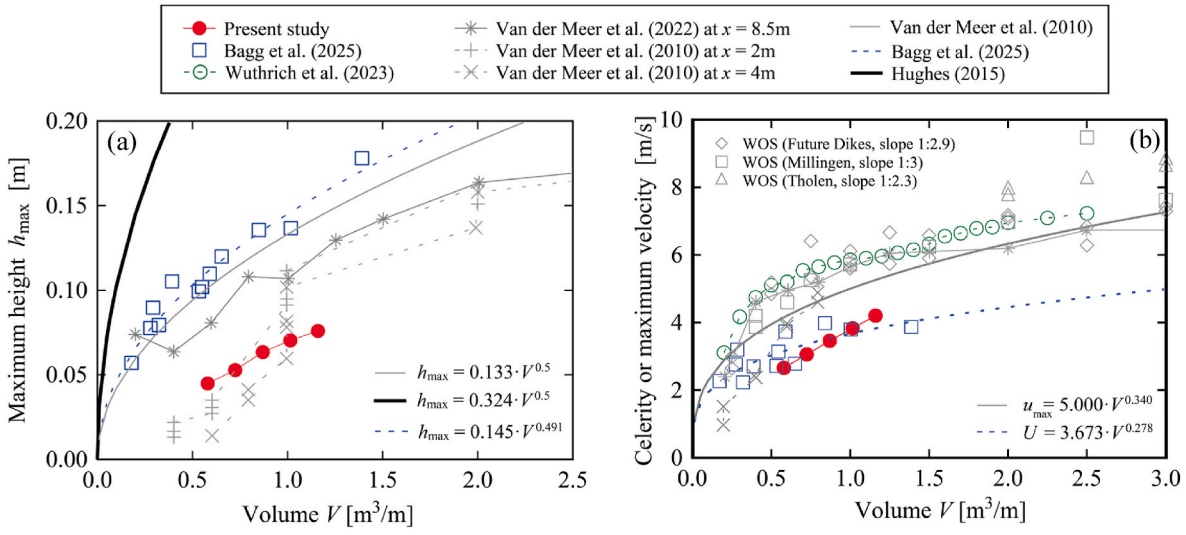


Fig. 11. Comparison of present dam-break data with previous studies on overtopping waves (WOS) on a slope for: (left) maximum wave height h_{max} and (right) wave front celerity or maximum velocity. Where relevant, present data at $x = 3.8$ m (slope 1:3) are compared with literature, including Van der Meer et al. (2010) at $x = 2$ m and 4 m (slope 1:3.7), Van der Meer et al. (2022) at x = 8.5 m (slope 1:3), Hughes (2015) and (Wüthrich et al., 2022) at $x = 6$ m (slope 1:3). For completeness, experimental velocities of tests conducted in FutureDikes, Millingen and Tholen are also plotted , with test conditions summarized in Table 1.

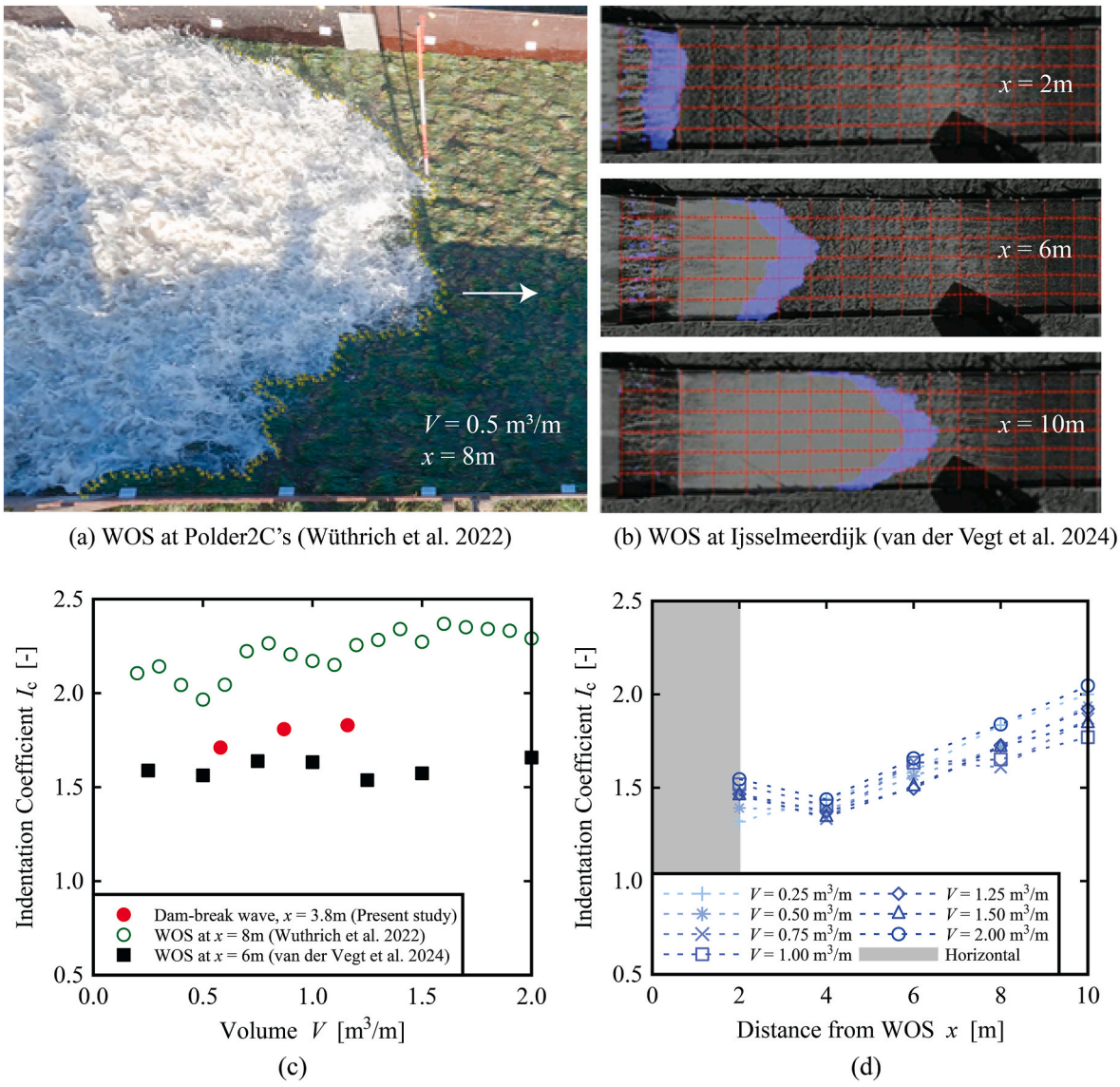


Fig. 12. Indentation coefficient I_c of WOS-generated waves and comparison with dam-break waves. (top) Photographs of overtopping waves and corresponding perimeter measurements for: (a) Polder2C's (Wüthrich et al., 2022) and (b) Ijsselmeerdijk (van der Vegt et al., 2024), where only the first 10 m with a slope of 1:3 are considered. (bottom) (c) Comparison of I_c for WOS and laboratory dam-break waves at $x = 3.8$ m. Data from Wüthrich et al. (2022) were collected at $x = 8$ m; while for the WOS tests at Ijsselmeerdijk, measurements were taken at $x = 6$ m, corresponding to a 4 m slope section (the first 2 m being horizontal), identified as the most representative location. (d) Indentation coefficients for various released volumes in the WOS experiments at Ijsselmeerdijk.

$x = 8$ m from the WOS, slightly higher values were found, with $I_c \sim 2$ for smaller volumes, increase towards 2.4 for larger ones (Fig. 12c). The indentation coefficients at selected longitudinal (streamwise) positions are compared in Fig. 12c, showing good agreement between dam-break waves and WOS experiments at Ijsselmeerdijk, whereas *Polder2C*'s data exhibited systematically higher values, possibly due to the larger distance from the crest ($x = 8$ m) as well as the presence of larger macro-roughness and irregularities in the real grass found in the field. However, despite these differences, prototype WOS values of I_c are generally higher than those obtained in the laboratory. This can be attributed to multiple factors, including larger roughness effects (as discussed in Section 5.3), and (up)scaling limitations, since not all air-water flow properties are accurately reproduced between laboratory and prototype (Estrella et al., 2022; Chanson and Wüthrich, 2025; Regout et al., 2026). Differences in image resolution and pixel size might also contribute to the discrepancies, as well as variations in flume width. However, a more definitive assessment would require additional experiments in large-scale facilities to better quantify and isolate these effects.

While these comparisons provide valuable insights, they remain qualitative, since the hydrodynamic characteristics of these unsteady flows are affected by multiple factors (including release mechanisms and outflow conditions at the gate), which are not always directly comparable. Furthermore, data for individual overtopping waves remain scarce (Bagg et al., 2025). More specifically, the relationship between released volume V (in m³/m) and initial water level in the reservoir (or storage tank, in m) directly affects the outflow conditions, and thus the flow behaviour in the various set-ups. For WOS 2.0 (the simulator in use since 2019) the relationship between released volume and reservoir water level was obtained from construction drawings by *Van der Meer Innovation*, as presented by Van Leent (2026). These data indicate that WOS and dam-break facility exhibit very different relationships between volumes V and initial water levels, or impoundment depths d_0 for dam-break waves (Fig. 13). For example, at a reservoir height of 0.4 m, the WOS releases a small volume of ~0.16 m³/m, while the corresponding dam-break volume in Table 2 would be 1.16 m³/m. These

differences in the release characteristics, combined with the fact that overtopping volumes go through a transition from valve opening to a horizontal flow of water at the crest of a levee before descending the slope (whereas dam-break waves are released directly on the slope), likely contribute to the differences observed in Figs. 11 and 12. In addition, for WOS the shape of the water tank of the overtopping simulator depends on the flow velocities required at the crest of the levee, while for dam-break waves the geometry remains constant (Fig. 13). Overall, it is important to acknowledge that these limitations limit any direct (quantitative) comparison between the two flow types, for which additional research is needed, possibly including comparison with data from real life overtopping events.

This analysis also shows the need for further research on the evolution of these unsteady flows along (vegetated) slopes, regardless of their generation mechanism, as this significantly influences key processes, including overtopping on coastal and riverine structures, with the latter often affected by lower volumes. More specifically, air entrainment plays a crucial role in modifying flow density and affecting the complex recirculation dynamics within the breaking roller (e.g. Regout et al., 2025). These effects may have implications for erosion and scour on coastal and riverine dikes: critical topics that warrant further attention from hydraulic and coastal engineers.

7. Conclusion

Coastal processes are governed by unsteady and rapidly changing dynamics that require a deeper physical understanding, critical for the design and assessment of flood defences. This study presents an experimental investigation of highly unsteady flows in the form of dam-break waves, propagating over smooth and grass-covered slopes, representative of coastal and river dikes. These new experiments offer valuable insights into the hydrodynamics of unsteady dam-break waves, enabling meaningful comparison with overtopping waves.

The sudden release of an impounded water volume generated a dam-break wave that propagated along a 1:3 downward slope, equipped with ultrasonic distance sensors and high-speed imaging to capture flow depth, front celerity and air-water interactions. On smooth slopes, the dam-break wave advanced rapidly with a sharp front and limited aeration. In contrast, surface roughness and the grass-covered slope substantially influenced wave propagation, resulting in lower celerities and a highly aerated "*white-water*" front. Visual observations showed that this aerated region was not confined to the wave tip region, but extended upstream and evolved in space and time, emphasizing the spatially distributed nature of air entrainment. Empirical relationships were proposed to quantify the length of the aerated region up to 5 times the dam's impounded depth, pointing out the need for additional, more quantitative, air-water measurements. Front celerities were consistent with Hunt's (1982) analytical solution for dam-break waves on slopes with friction factors between $f = 0.02$ and 0.2, in line with previous studies. The results revealed two distinct flow propagation phases: an initial acceleration phase dominated by gravity, followed by a decelerating phase in which friction progressively became the controlling factor, ultimately approaching conditions consistent with steady flow conditions. Ensemble-averaged water surface profiles, obtained from up to 320 repetitions, showed a characteristic shape with a front tip and rising limb followed by a gradual decline. This statistical approach enabled the quantification of free-surface variability, showing that surface fluctuations remained relatively constant throughout the wave, with the largest variations during the rising limb, close to the maximum depth. The indentation coefficient I_c (defined as the ratio between the roller perimeter and the channel width) was used to describe the degree of three-dimensionality of the flow. Smooth slopes exhibited lower values $I_c \sim 1.3$, while grass-covered slopes showed larger and progressively increasing values along the chute, reaching approximately $I_c > 1.8$.

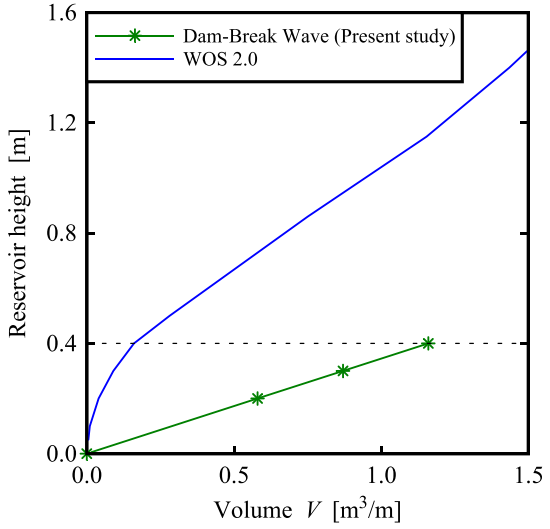


Fig. 13. Relationship between released volume V and initial water level in the reservoir (e.g. d_0 for dam break waves). Data for WOS 2.0 is based on construction drawings by *Van der Meer Innovation*, as presented by Van Leent (2026).

While these findings advance our physical understanding of unsteady aerated flows over grass slopes, they also enable a meaningful comparison between dam-break and wave overtopping events, extending the work by Bagg et al. (2025). Results revealed strong visual similarities in aeration patterns, front structure, and roughness effects. Measured water depths and wave-front celerities were generally lower than those observed for WOS-generated waves, though they remained of comparable magnitude. The indentation coefficients exhibited strong qualitative agreement with large-scale overtopping data, with both showing an increasing trend along the slope. However, differences in release conditions, geometries, and scaling effects limit the possibility of direct quantitative comparison.

Future research should investigate the evolution of these waves along the slope, with particular attention to the roles of air entrainment and roughness, which both critically influence overtopping dynamics and stability of coastal protections. A better understanding of the air-water nature of these flows is also important for interpreting erosion mechanisms. In this context, the present experimental data can support the development and validation of numerical and analytical models, contributing to the development of more reliable and resilient design strategies for coastal structures.

Declaration of generative AI and AI-assisted technologies in the manuscript preparation process

During the preparation of this work the author(s) used ChatGPT in order to reformulate text and improve readability. After using this tool/service, the author(s) reviewed and edited the content as needed and take(s) full responsibility for the content of the published article.

CRediT authorship contribution statement

Davide Wüthrich: Conceptualization, Data curation, Formal analysis, Funding acquisition, Investigation, Methodology, Project administration, Writing – original draft. **Anne Mozer:** Conceptualization, Data curation, Formal analysis, Investigation, Methodology, Validation, Writing – review & editing. **Holger Schüttrumpf:** Funding acquisition, Project administration, Supervision, Writing – review & editing.

Declaration of competing interest

The authors declare that they have no known competing financial

interests or personal relationships that could have appeared to influence the work reported in this paper.

Acknowledgements

The authors acknowledge the IDEA League Fellowship for supporting collaboration between TU Delft and RWTH Aachen. The financial support of the project (Funding code: 471796635) of the German Research Foundation (DFG) is acknowledged. We thank the IWW laboratory technicians for their assistance during the experiments. We thank Prof. Hubert Chanson (University of Queensland, Australia), Dr. Elena-Maria Klopries, Dr. Harish Selvam and Ms. Lisa Burghardt (RWTH Aachen University, Germany), Dr Bas Hofland, Dr Juan Aguilar Lopez, Ir. Niels van der Vegt and Ir. Simon van Leent (TU Delft, the Netherlands) for the insightful discussions that contributed to this work. We also thank Infram for providing access to the *FutureDikes* experimental data.

List of symbols

B	channel width, here $B = 0.5$ [m]
d_0	dam's impoundment depth [m]
f	Darcy friction factor [−]
g	gravitational constant $g = 9.81$ [m/s^2]
h	flow depth [m]
h_0	flow depth at the gate ($x = 0$) [m]
h_{max}	maximum wave height [m]
I_c	indentation coefficient, defined as $I_c = L_{roller}/B$ [−]
L	length of the reservoir according to Hunt, $L = S_0/d_0$ [m]
L_{air}	length of the aerated front region [m]
L_{roller}	length of the roller perimeter in the transversal direction [m]
n	Manning friction coefficient [s/m$^{1/3}$]
Q	discharge [m^3/s]
q_0	unit discharge at the gate ($x = 0$) $q_0 = Q_0/B$ [m^2/s]
Q_0	discharge at the gate ($x = 0$) [m^3/s]
Re	Reynolds number, defined as Re $= \rho h v/\mu$ [−]
S_0	slope [−]
T	synchronised time [s]
t	time [s]
T_{max}	synchronised time when h_{max} occurs [s]
$T_{m\text{-}1,0}$	period of overtopped waves [s]
U	wave front celerity [m/s]
U_{US}	wave front celerity measured with US [m/s]
v	flow velocity [m/s]
v_0	flow velocity at the gate ($x = 0$) [m/s]
V	volume per unit length [m^3/m]
V_H	uniform equilibrium flow velocity [−]
x	longitudinal (streamwise) coordinate [m]
x_s	position of the wave front [m]
y	vertical coordinate [m]
z	transversal coordinate [m]
μ	dynamic viscosity, $\mu = 1.002{\cdot}10^{-3}$ [Pa·s]
ρ	water density $\rho = 1\,000$ [kg/m^3]
σ	standard deviation

Data availability

Data will be made available on request.

References

Ancey, C., Iverson, R.M., Rentschler, M., Denlinger, R.P., 2008. An exact solution for ideal dam-break floods on steep slopes. Water Resour. Res. 44 (1), W01430.
Bagg, J., Battley, M., Whittaker, C., Shand, T., 2025. Application of laboratory dam break experiments to non-impulsive wave overtopping. Coast. Eng. 198, 104695.
Bakker, J., Melis, R., Mom, R.J.C., 2013. Factual Report: Overslagproeven Rivierenland (Dutch) [Factual Report: Wave Overtopping Experiments Waterboard Rivierenland]. Technical Report 12i071. Infram.
Bakker, J., Mom, R.J.C., Steendam, G.J., Van der Meer, J.W., 2011. Factual report. Overslagproeven en oploopproef Tholen (Dutch) [Factual Report. Wave overtopping and runup experiments Tholen]. Technical Report 10i092. Infram.
Brocchini, M., Peregrine, D., 2001. The dynamics of strong turbulence at free surfaces. Part 1. Description. J. Fluid Mech. 449, 225–254.
Chanson, H., 1994. Drag reduction in open-channel flow by aeration and suspended load. J. Hydraul. Res. 32 (1), 87–101.
Chanson, H., 2005. Air–water and momentum exchanges in unsteady surging waters: an experimental study. Exp. Therm. Fluid Sci. 30 (1), 37–47.
Chanson, H., 2006. Tsunami surges on dry coastal plains: application of dam break wave equations. Coast. Eng. J. 48 (4), 355–370.
Chanson, H., 2009. Application of the method of characteristics to the dam break wave problem. J. Hydraul. Res. 47 (1), 41–49.
Chanson, H., 2024. Self-aeration on large dam spillways during major floods. J. Hydroenviron. Res. 54, 26–36.
Chanson, H., 2004a. Unsteady air-water flow measurements in sudden open channel flows. Exp. Fluid 37 (6), 899–909.
Chanson, H., Wüthrich, D., 2025. Discussion of 'Air water flows' by Daniel Valero, Stefan Felder, matthias kramer, Hang Wang, José M. Carrillo, Michael Pfister and Daniel B. Bung. J. Hydraul. Res. 63 (3), 401–404.
Chanson, H., 2004b. Experimental study of flash flood surges down a rough sloping channel. Water Resour. Res. 40 (3), W03301.
Chen, C.L., Armbruster, J.T., 1980. Dam-break wave model: formulation and verification. J. Hydraul. Div. 106 (5), 747–767.
Daamen, E., Heida, L., Mom, R.J.C., Overduin, M., Wauben, C., 2023. Factual Report. Praktijkproeven Future Dikes (Dutch) [Factual report. Field Experiments Future Dikes]. *Technical Report 21i873*. Infram. V2.0.
DIN 19712, 2013. Hochwasserschutzanlagen an Fließgewässern (Flood Protection Works on Rivers). Beuth-Verlag, Berlin, Germany.
Dressler, R.F., 1952. Hydraulic resistance effect upon the dam-break functions. J. Res. 49 (3), 217–225. National Bureau of Standards.
Dressler, R.F., 1958. Unsteady Non-linear Waves in Sloping Channels, 247. Proc. Royal Society of London, SeriesA, pp. 186–198.
Escande, L., Nougaro, J., Castex, L., Barthet, H., 1961. Influence de Quelques Paramètres sur une Onde de Crue Subite à l'Aval d'un Barrage. La Houille Blanche 5, 565–575.
Estrella, J., Wüthrich, D., Chanson, H., 2022. Two-phase air-water flows in hydraulic jumps at low froude numbers: similarity, scale effects and need for field observations. Exp. Therm. Fluid Sci. 130, 110486.
EurOtop, 2018. Manual on Wave Overtopping of Sea Defences and Related Structures. URL. www.overtopping-manual.com.
Froehlich, D.C., 2016. Predicting peak discharge from gradually breached embankment dam. J. Hydrol. Eng. 21 (11), 04016041.
Goda, 2000. Random seas and design of maritime structures. In: Advanced Series in Coastal Engineering, 15. World Scientific. ISBN 981-02-3256-X.
Hamlet, A.F., Lettenmaier, D.P., 2007. Effects of 20th century warming and climate variability on flood risk in the western U.S. Water Resour. Res. 43 (6), W06427.
Hughes, S.A., 2015. Hydraulic parameters of overtopping wave volumes. Coastal Structures and Solutions to Coastal Disasters 2015, pp. 710–718.
Hughes, S.A., Thornton, C.I., 2016. Estimation of time-varying discharge and cumulative volume in individual overtopping waves. Coast. Eng. 117, 191–204.
Hunt, B., 1982. Asymptotic solution for dam-break problem. J. Hydraul. Div. 108 (1), 115–126.
Hunt, B., 1984. Perturbation solution for dam break floods. J. Hydraul. Eng. 110 (8), 1058–1071.
Idelchik, I.E., 1969. Mémento des pertes de charge. Eyrolles Editor, *Collection De La Direction Des Études Et Recherches D'Electricité De France*. Paris, France (in French).
Lauber, G., Hager, W.H., 1998. Experiments to dam-break wave: sloping channel. J. Hydraul. Res. 36 (5), 761–773.
Liu, W., Wang, B., Guo, Y., Zhang, J., Chen, Y., 2020. Experimental investigation on the effects of bed slope and tailwater on dam-break flows. J. Hydrol. 590, 125256.
Melis, M., Poggi, D., Fasanella, G.O.D., Cordero, S., Katul, G.G., 2019. Resistance to flow on a sloping channel covered by dense vegetation following a dam break. Water Resour. Res. 55 (2), 1040–1058.
Mozer, A., Harish, S., Schüttrumpf, H., 2025. Determining aeration properties over vegetated embankments. Phys. Fluids 37 (12).
Mozer, A., Harish, S., 2024. Investigating the influence of vegetation height on the air concentration of supercritical aerated flows. Water 16 (21), 3136.
Mungkasi, S., Roberts, S.G., 2011. A new analytical solution for testing debris avalanche numerical models. ANZIAM J. 52 (CTAC2010), C349–C363.
Nielsen, P., Xu, B., Wüthrich, D., Zhang, S., 2022. Friction effects on quasi-steady dam-break wave propagation on horizontal beds. J. Fluid Mech. 939, A21.
Nsom, B., Debiane, K., Piau, J.M., 2000. Bed slope effect on the dam break problem. J. Hydraul. Res. 38 (6), 459–464.
Regout, D., Jonkman, S.N., Wüthrich, D., 2025. Experimental study of air–water flow properties in the breaking roller of dam-break waves. Int. J. Multiphas. Flow 185, 105119.
Regout, D., van Nieken, A., Wüthrich, D., 2026. Multi-scale analysis of air-water properties and free-surface dynamics in dam-break waves. Exp. Therm. Fluid Sci. 177, 111782.
Ritter, A., 1892. Die Fortpflanzung der Wasserwellen. Zeitschrft des Vereines Deutscher Ingenieure 36 (33), 947–954.
Sakkas, J., Strelkoff, T., 1973. Dam-break flood in a prismatic dry channel. J. Hydraul. Div. 99 (HY12), 2195–2216 (Paper 10233).

Sakkas, Strelkoff, T., 1976. Dimensionless solution of dam-break flood waves. J. Hydraul. Div. 102 (HY2), 171–184 (Paper 11910).
Schüttrumpf, H., Oumeraci, H., 2005. Layer thicknesses and velocities of wave overtopping flow at seadikes. Coast. Eng. 52 (6), 473–495.
Stansby, P., Chegini, A., Barnes, T., 1998. The initial stages of dam-break flow. J. Fluid Mech. 374, 407–424.
Stoker, J.J., 1957. Water Waves: the Mathematical Theory with Applications. John Wiley & Sons, New York.
van Bergeijk, V.M., Warmink, J.J., Hulscher, S.J.M.H., 2020. Modelling the wave overtopping flow over the crest and the landward slope of grass covered flood defences. J. Mar. Sci. Eng. 8, 489.
Van der Meer, J.W., 2007. Design, construction, calibration and use of the wave overtopping simulator. Technical Report. ComCoast-Infram. http://resolver.tudelft.nl/uuid:5656bf8b-e799-4c7f-87d4-82d4f8a26fef.
Van der Meer, J., Steendam, G.J., Bruce, T., Klein Breteler, M., 2022. Admissible post-wave overtopping flow for persons on a horizontal surface. Journal of Coastal & Hydraulic Structures 2.
Van der Meer, J.W., Bernardini, P., Steendam, G.J., Akkerman, G.J., Hoffmans, G., 2007. The wave overtopping simulator in action. Coastal Structures 2007, pp. 645–656.
Van der Meer, J.W., Hardeman, B., Steendam, G.J., Schüttrumpf, H., Verheij, H., 2010. Flow depths and velocities at crest and landward slope of a dike, in theory and with the wave overtopping simulator. Coast. Eng. Proc. 1 (32).
van der Vegt, N., Hofland, B., van Bergeijk, V.M., Hulscher, S.J.M.H., Warmink, J.J., 2026. Spatiotemporal numerical modeling of wave overtopping flow over dike crests and landward slopes. Appl. Ocean Res. 168, 104972.
van der Vegt, N., Huis in 't Veld, M., van der Meer, J., 2024. Analyse overslagproeven IJsselmeerdijk. Achtergrondrapportage innovatieproject: Verhogen Erosiebestendigheid Overgangen Dijkbekleding. Concept Report PR4824 10 [in Dutch].
van Leent, S.J., 2026. Simulating Overtopping Waves on a Landward Dike Slope. Msc Thesis. Delft University of Technology.
Wang, L.H., Pan, C.H., 2015. An analysis of dam-break flow on slope. J. Hydrodyn. Ser. B 26 (6), 902–911.
Whitham, G.B., 1955. The Effects of Hydraulic Resistance in the Dam-Break Problem, 227. *Proceeding of the Royal Society of London*, Series A, pp. 399–407.
Wüthrich, D., Pfister, M., Nistor, I., Schleiss, A.J., 2018. Experimental study of tsunami-like waves generated with a vertical release technique on dry and wet beds. J. Waterw. Port, Coast. Ocean Eng. 144 (4), 04018006.
Wüthrich, D., Pfister, M., Schleiss, A.J., 2019. Effect of bed roughness on tsunami-like waves and induced loads on buildings. Coast. Eng. 152, 103508.
Wüthrich, D., Rikkert, S.J., Lanzafame, R., 2022. Human stability on slopes under overtopping waves. Coast. Eng. Proc. (37) 129-129.
Wüthrich, D., Shi, R., Chanson, H., 2020. Physical study of the 3-dimensional characteristics and free-surface properties of a breaking roller in bores and surges. Exp. Therm. Fluid Sci. 112, 109980.
Wüthrich, D., Shi, R., Chanson, H., 2021. Strong free-surface turbulence in breaking bores: a physical study on the free-surface dynamics and air–water interfacial features. J. Fluid Mech. 924, A20.
Wüthrich, D., Shi, R., Chanson, H., 2022a. Ensemble-statistical approach in the measurement of air-water flow properties in highly unsteady breaking bores. Rev. Sci. Instrum. 93 (5).
Xu, B., Shi, R., Nielsen, P., Gong, Z., 2023. Experimental investigation into the boundary layer structure near the tip of a dam-break wave on a dry, rough and horizontal bed. Coast. Eng. 179, 104252.